GEOCHEMISTRY

Beyond the tropopause hypothesis: Drivers of even mercury isotope fractionation unraveled by 3D modeling

Zhengcheng Song[1,2]*, Shaojian Huang[1], Peng Zhang[1], Tengfei Yuan[3], Xin Miao[1], Kaihui Tang[4], Guangyi Sun[4], Xuewu Fu[4], Ruoyu Sun[5], Wang Zheng[5], Jiubin Chen[5], Yanxu Zhang[3]*

Mercury (Hg) is a globally persistent contaminant with substantial health impact. The mass-independent fractionation of even mercury isotopes (even-MIF, denoted as Δ^{200}Hg) is widely used to trace atmospheric Hg sources and fluxes. However, the chemical processes inducing even-MIF remain largely unknown. Here, we develop a three-dimensional atmospheric Hg isotope model linking Hg redox processes with even-MIF. The results show that the previous hypothesis of even-MIF occurring exclusively at the tropopause may not fully explain the global Δ^{200}Hg patterns. We speculate OH-initiated reactions and photoreduction of Hg^{II}(p) as likely dominant drivers. Simulations show that even-MIF primarily originates in the free troposphere and propagates downward to surface air. Our results reveal distinct spatial Δ^{200}Hg variations that were previously unaccounted for in tracing Hg sources. This study provides critical insights into even-MIF drivers and serves as a reference for using Δ^{200}Hg to trace atmospheric Hg sources.

INTRODUCTION

Mercury (Hg) is a potent neurotoxin that adversely affects human health, wildlife, and ecosystems worldwide (*1*). Anthropogenic activities, such as fossil fuel combustion and metal mining, have substantially increased Hg emissions, leading to widespread environmental Hg contamination since the industrial era (*2*, *3*). The atmosphere, serving as a medium for Hg transport and deposition, is the primary source of Hg to both the ocean and land (*4*). Stable Hg isotopes can elucidate atmospheric sources (*5*–*7*), typically exhibiting distinct mass-dependent fractionation (MDF; δ^{202}Hg) and mass-independent fractionation for odd mass isotopes (odd-MIF; Δ^{199}Hg and Δ^{201}Hg) and even mass isotopes (even-MIF; Δ^{200}Hg and Δ^{204}Hg) for different Hg species. MDF occurs in almost all physical and chemical processes, while the odd-MIF mainly associated with photochemistry processes (*8*, *9*). The even-MIF is assumed generated in the upper troposphere and/or tropopause through photochemical reactions and is considered as a conservative tracer in the lower atmosphere and extensively used for tracing atmospheric inputs of Hg (*10*–*12*). However, such an assumption has not been evaluated globally and the specific processes and mechanism of even-MIF remains largely unknown (*8*, *9*).

Early studies suggested that even-MIF is induced by photochemical reactions of Hg in the upper atmosphere. Notable positive Δ^{200}Hg (up to 1.2‰) was first observed in precipitation and snow in North America (*12*–*15*) and suggested to be triggered by photo-initiated oxidation of Hg^0 occurring on aerosol or solid surfaces in the tropopause (*11*, *12*). Positive Δ^{200}Hg (~0.2‰) was also reported in both gaseous Hg^{II} and precipitation at high-altitude sites (*10*) and suggested to occur via Hg^{I} and Hg^{II} photolysis on aerosols involving magnetic halogen nuclei. Recent studies have also reported positive Δ^{200}Hg values (~0.1 to 0.2‰) in surface urban and marine aerosol, but the correlation with the upper atmosphere remains unclear, adding complexity to the explanation of observed even-MIF in the atmosphere (*16*–*20*).

Experimental studies have suggested the Hg^0 + Cl reaction and the photodissociation of mercuric oxides in the ultraviolet C (UVC)–irradiated Hg-O_2 system as triggers for even-MIF (*21*, *22*). Theoretically, the nuclear volume effect may cause small even-MIF (*23*, *24*). A molecular magnetic isotope effect is also supposed to induce even-MIF (*10*), but this effect is limited in the aqueous phases, as water is required to hydrate the Hg-ligand radical pairs produced by photolysis, creating a cage effect that can extend the lifetime of the radical pair sufficiently for fractionation (*25*–*27*). Other studies have also discussed the possibility of even-MIF caused by self-shielding (*28*) and neutron capture (*11*). However, the magnitude of these effects is much lower than the observed variability of even-MIF in the environment. These studies are challenging due to the complexity of atmospheric Hg chemical processes, which are difficult to isolate and replicate accurately in laboratory settings. In addition, the atmospheric transport, mixing, and deposition processes can disperse even-MIF signals far from their locations of origin, adding further complexity to their interpretation.

Here, we synthesized isotopic signatures from Hg emission sources and even-isotopic fractionation during redox processes to develop a comprehensive model representation of the even-MIF in the atmosphere based on the GEOS-Chem platform. The model accounts for the transport of individual Hg isotopes, their anthropogenic and natural emissions (*29*, *30*) (Table 1), chemical transformations, isotope fractionation, and both dry and wet depositions (*31*, *32*). It incorporates the latest chemical mechanisms that propose over 30 redox reactions that are categorized into four redox pathways (*29*): three oxidation pathways converting Hg^0 to Hg^{II}—initiated by bromine (Br), Chlorine (Cl) and hydroxyl radicals (OH)—and a key photoreduction pathway of Hg^{II} in heterogeneously particulate matter

[1]School of Atmospheric Sciences, Nanjing University, Nanjing, Jiangsu 210023, China. [2]Frontiers Science Center for Critical Earth Material Cycling, Nanjing University, Nanjing, Jiangsu 210023, China. [3]Department of Earth and Environmental Sciences, Tulane University, New Orleans, LA 70118, USA. [4]State Key Laboratory of Environmental Geochemistry, Institute of Geochemistry, Chinese Academy of Sciences, Guiyang 550081, China. [5]School of Earth System Science, Institute of Surface-Earth System Science, Tianjin University, Tianjin 300072, China.
*Corresponding author. Email: songzc@nju.edu.cn (Z.S.); yzhang127@tulane.edu (Y.Z.)

Table 1. Mercury fluxes and mean Δ^{200}Hg signatures of source emissions.

Sources*	Anthropogenic†	Soil‡	Ocean§	Biomass‖	Geogenic¶
Flux (Gg year^{-1})	2.20	0.85	4.80	0.30	0.30
Δ^{200}Hg (‰)	0.00	−0.01	0.04	−0.04	0.00
1 SD (‰)	0.03	0.03	0.05	0.02	0.02

*Both anthropogenic and natural Hg emission fluxes are from references (*29*, *34*). †Anthropogenic released Δ^{200}Hg signatures are cited from Sun *et al.* (*60*,*74*). ‡Δ^{200}Hg signature for soil emission is adopted from Sun *et al.* (*60*) and Wang *et al.* (*75*). §The Δ^{200}Hg signature for ocean emission is assumed consistent with that in oceanic samples, as synthesized in Jiskra *et al.* (*5*). ‖Δ^{200}Hg signature for biomass emission is compiled from references (*44*,*46*, *76*–*79*). ¶Δ^{200}Hg signature for geogenic emission are cited from volcanic emissions reported by Sun *et al.* (*74*).

[Hg^{II}(p)] (see Materials and Methods) (*29*). These chemical processes incorporate recent laboratory and computational findings and have been extensively evaluated against observations (*29*, *31*).

We performed scenarios simulation experiments to evaluate redox pathways capable of reproducing the globally observed atmospheric Δ^{200}Hg signatures (fig. S1). Global measurements of mean Δ^{200}Hg values for various Hg species and their spatial variability were used to assess the model output. The enrichment factor (*E*), defined as the ratio of product to reactant and reflecting the enrichment of Δ^{200}Hg in Hg^{II} and the depletion in Hg^0 during redox reactions, was treated as a variable to account for its uncertainty. First, based on early even-MIF theory, we assumed that even-MIF is generated solely by Hg^0 oxidation in the tropopause (interlayer between the stratosphere and the troposphere) (*11*, *12*). Second, we examined all redox processes to identify those capable of reproducing the observations. Third, we refined the simulations by adjusting enrichment factors to achieve optimal agreement with the global data. The optimal simulation identified OH-initiated oxidation and Hg^{II}(p) photoreduction as the most plausible pathways responsible for even-MIF in the atmosphere. Finally, we revealed the spatial distribution of global Δ^{200}Hg signatures and assessed their potential as tracers for atmospheric Hg sources.

RESULTS

Hg oxidation above the tropopause is insufficient to explain the observations

Our initial simulation experiment examined the hypothesis that even-MIF is generated exclusively through Hg^0 oxidation in the tropopause, as proposed by previous studies (*11*, *12*). To restrict even-MIF to the tropopause, we leveraged the model's ability to identify the tropopause layer using meteorological data and applied isotopic fractionation factors specifically to Hg^0 oxidation occurring within that layer. We evaluated our simulations against two observational constraints: (i) the mean Δ^{200}Hg values for Hg^0, Hg^{II}(p), Hg^{II}(g), and Hg^{II}(pre) and (ii) their spatial variability. As the enrichment factors for these chemical reactions remain undetermined, we varied *E* over a range from 2.6 to 260‰ to test the simulation sensitivity and compared the results with observations (Fig. 1). At a low enrichment factor [*E* = 2.6‰, corresponding to 10 times the observed net oxidation factor (*10*)], the model failed to capture the Δ^{200}Hg gradients across different Hg species. Specifically, the simulated mean Δ^{200}Hg values converged toward a similar average, falling above the observed values for Hg^0 ($\Delta^{200}Hg^0$) but below those for Hg^{II}(p, g) [$\Delta^{200}Hg^{II}$(p, g)] and Hg^{II}(pre) [$\Delta^{200}Hg^{II}$(pre)]. When the *E* was increased by an order of magnitude (*E* = 26 and 40‰), the modeled Δ^{200}Hg values for the various Hg species began to diverge: $\Delta^{200}Hg^0$ trended negative, $\Delta^{200}Hg^{II}$(p, g) approached zero, and $\Delta^{200}Hg^{II}$(pre) shifted toward positive values (Fig. 1A). However, although the simulated mean values approximately to the observations when accounting for standard deviations (Fig. 1, A and B), the spatial distributions of Δ^{200}Hg in Hg^{II}(p), Hg^{II}(g), and precipitation remained inconsistent with the observations (Fig. 1C and fig. S2).

The spatial distribution patterns of the modeled results remained relatively invariant to changes in the enrichment factors (fig. S2). Consequently, the correlation coefficients (*r*) between the modeled and observed Δ^{200}Hg values were stable at ~0.7 for Hg^0 ($P < 0.01$), 0.3 for Hg^{II} ($P = 0.42$), and 0.2 ($P = 0.44$) for Hg^{II}(pre) (Fig. 1C). Although Δ^{200}Hg in Hg^0 showed a strong positive correlation, the variability trends for the simulated Δ^{200}Hg in Hg^{II} and Hg^{II}(pre) deviated markedly from observations, especially for the latitudinal variation of $\Delta^{200}Hg^{II}$(pre) (fig. S3). This is particularly important because observational data indicate that Hg^{II} and precipitation are most affected by the even-MIF effect. Also wet deposition, originating from the upper atmosphere, provides the most representative data for even-MIF in that region. At higher enrichment factors (e.g., *E* = 260‰), although elevated Δ^{200}Hg signatures in the upper atmosphere may influence the lower atmosphere (figs. S2 and S4), the simulations could not concurrently reproduce both the mean Δ^{200}Hg values and the spatial variability across different atmospheric Hg forms. Therefore, our modeling results suggest that the hypothesis of even-MIF occurring exclusively at the tropopause may not fully account for the global Δ^{200}Hg observations.

Moreover, recent research into stratospheric Hg chemistry has speculated on a stratospheric contribution to global even-MIF (*33*) based on the theory that even-MIF may be induced during photolysis of mercuric oxides under UV radiation (*21*). To evaluate this mechanism, we performed a sensitive simulation incorporating even-MIF exclusively during stratospheric Hg^0 oxidation process with a substantial enrichment factor (*E* = 200‰). While our model uses a simplified representation of stratospheric chemistry compared to recent work (*33*), it nonetheless captures the potential influence of stratospherically generated even-MIF on the lower atmosphere and surface deposition. However, the model failed to reproduce both species-specific Δ^{200}Hg values and spatial distribution patterns (fig. S5). Although the modeled mean $\Delta^{200}Hg^{II}$(p, g) (0.11 ± 0.25‰) approximates observations, the Δ^{200}Hg values associated with Hg^0 and wet deposition deviate substantially from the measured data (fig. S5), and the modeled spatial

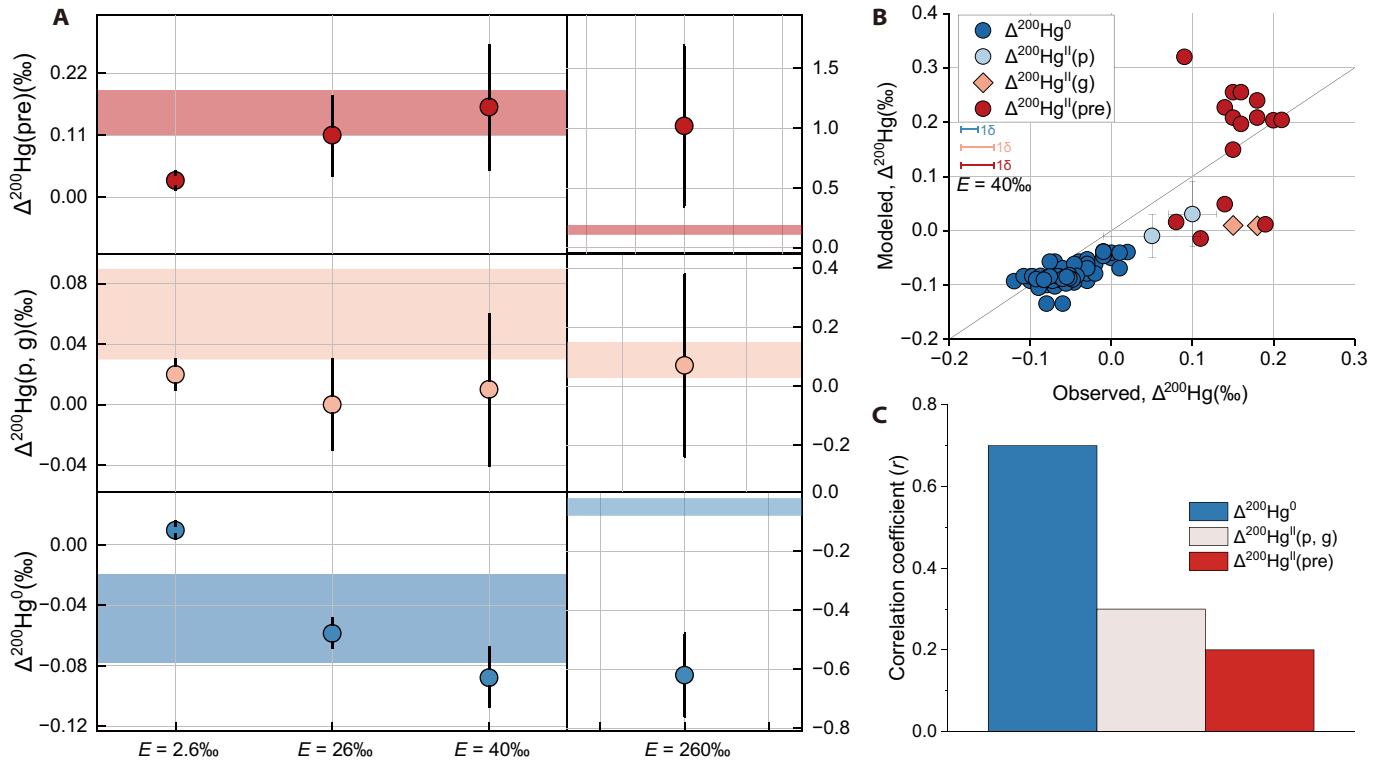

Fig. 1. Results comparison of observations and simulations when even-MIF is restricted in the tropopause layer. (**A**) Comparison of modeled mean Δ^{200}Hg values for Hg^0, Hg^{II}(p), and Hg^{II}(pre) (cycle symbols) with global observational data (shaded areas, means ± SD). Observed mean Δ^{200}Hg values are −0.05 ± 0.03‰ (Hg^0), 0.09 ± 0.06‰ [Hg^{II}(p, g)], and 0.15 ± 0.04‰ [Hg^{II}(pre)]. (**B**) Modeled versus observed Δ^{200}Hg values for atmospheric Hg species when even-MIF is applied to Hg^0 oxidation in the tropopause layer (E = 40‰). Error bars represent the reported SD of measured Δ^{200}Hg for: Hg^0 (blue), Hg^{II}(g) (yellow), and wet-deposited Hg^{II} (red) (1δ). Error bars for Hg^{II}(p) represent spatial variability in observational and modeled datasets. (**C**) Correlation coefficients (r) between modeled and observed Δ^{200}Hg values under the same even-MIF conditions (Hg^0 oxidation in the tropopause layer, E = 40‰).

variability of $\Delta^{200}Hg^{II}$(p, g) and $\Delta^{200}Hg^{II}$(pre) shows only a weak correlation with the observations. These results indicate that, regardless of the enrichment factor applied, the simulation fails to reproduce both the Δ^{200}Hg values and the spatial distribution of different Hg species. This suggests that an exclusively tropopause and stratospheric origin may not be the primary driver of global even-MIF. Nevertheless, the simulation does not include the most recent stratospheric Hg chemistry (*33*) and thus cannot definitively rule out the possibility of even-MIF being generated in the stratosphere.

Potential redox pathways inducing even-MIF

We systematically evaluated all relevant redox processes using state-of-the-art atmospheric Hg chemistry (*29*) to identify potential chemical processes inducing global even-MIF. We first assessed the sensitivity of simulated Δ^{200}Hg values to variations in enrichment factors applied on the same reaction. As shown in fig. S6, we selected three chemical reactions with enrichment factor of $|E| = 0.5$‰ and $|E| = 1.0$‰. The simulated Δ^{200}Hg values exhibited a strict linear relationship, indicating that while changes in the enrichment factor affect the magnitude of modeled Δ^{200}Hg values, they do not substantially alter their spatial distribution trends. Based on these findings, we used the observed spatial variability of Δ^{200}Hg data to constrain the simulation results for different chemical processes.

The Br-, Cl-, and OH-initiated pathways each comprise multiple oxidation and reduction reactions. We applied enrichment factors of $|E| = 1.0$‰ to each reaction separately and analyzed the correlation between simulated and observed Δ^{200}Hg values. As shown in Fig. 2 (A, B, and D), simulations involving Br-initiated, Cl-initiated, and Hg^{II}(g) photoreduction reactions failed to reproduce the spatial trends of Δ^{200}Hg for all three Hg forms, yielding low or even negative correlation coefficients (r) relative to the observations. The inability of these pathways to replicate the observed Δ^{200}Hg distributions likely reflects the spatial characteristics of their reaction sites, suggesting that Br- and Cl-initiated pathways are unlikely to be the primary drivers of global even-MIF. In contrast, simulations attributing even-MIF to OH-initiated reactions and Hg^{II}(p) photolysis exhibited strong correlations with observed Δ^{200}Hg values (Fig. 2, C and E). These results indicate that the spatial trends of Δ^{200}Hg values may depend on the underlying chemical pathways.

The OH-initiated pathway comprises a series of redox reactions. Our analysis revealed strong positive correlations between simulated Δ^{200}Hg values across different reactions in this pathway (fig. S7), suggesting that when even-MIF originates from any oxidation or reduction reaction within the pathway, the Δ^{200}Hg signal can propagate through subsequent redox steps and influences the final product. Consequently, the spatial distribution of Δ^{200}Hg values is highly similar across all OH-initiated reactions (Fig. 2C and fig. S7). This phenomenon suggests that, in our model, applying even-MIF to any reaction within the OH-initiated pathway is equivalent, as the existing observations do not constrain a specific reaction. To accurately identify the specific reactions

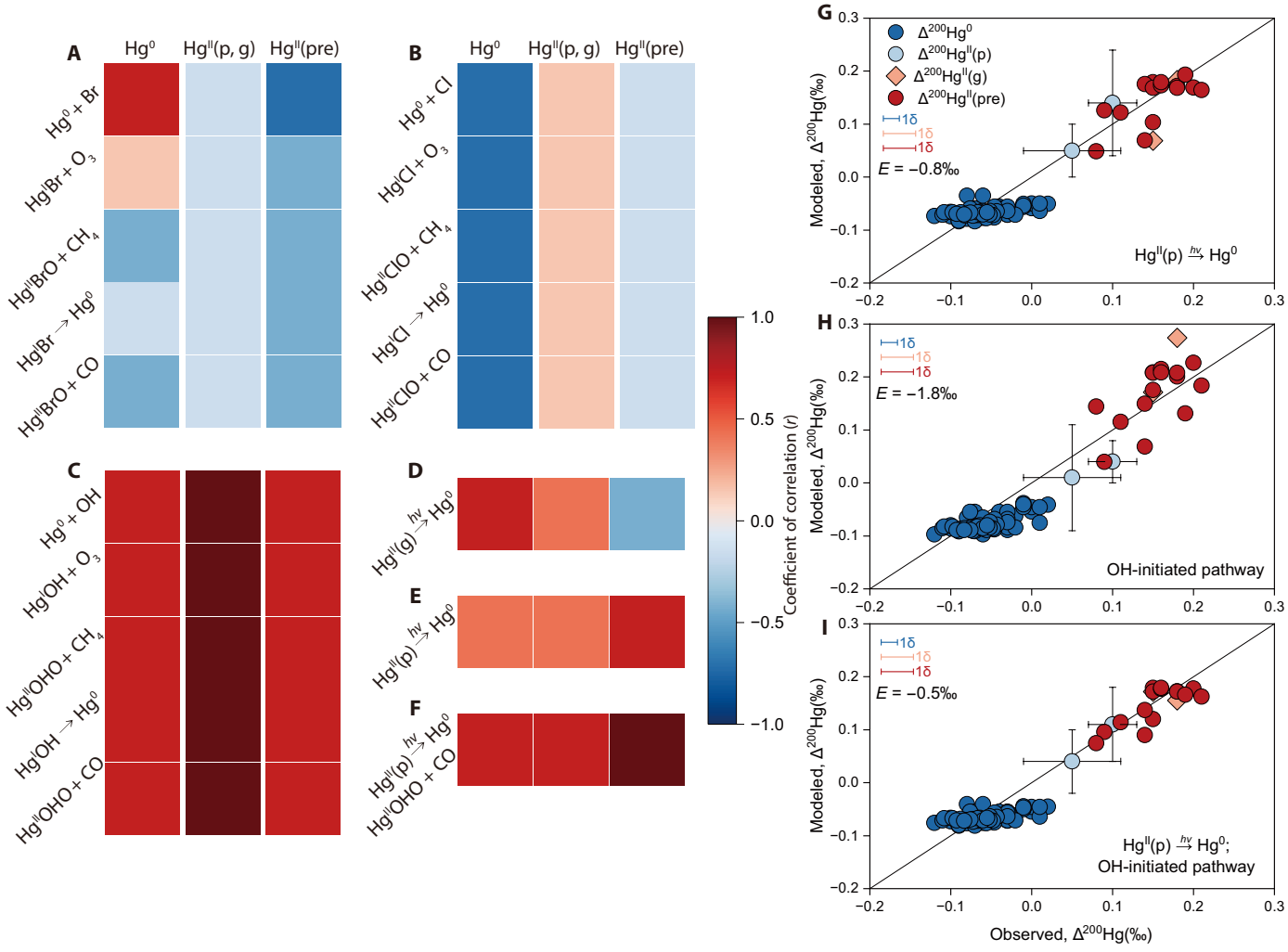

Fig. 2. Correlation coefficients (*r*) between modeled and observed Δ^{200}Hg values for atmospheric Hg species when even-MIF is applied (|*E*| = 1.0‰) to a specific chemical process. (**A**) Application of even-MIF to Br-initiated oxidation pathway. (**B**) Application of even-MIF to Cl-initiated oxidation pathway. (**C**) Application of even-MIF to OH-initiated oxidation pathway. (**D**) Application of even-MIF to Hg^{II}(g) photoreduction, which includes the photoreduction of all the gaseous Hg^{II} generated in Br-, Cl-, and OH-initiated reactions. (**E**) Application of even-MIF to Hg^{II}(p) photoreduction. (**F**) Combined application of even-MIF to OH-initiated oxidation and Hg^{II}(p) photoreduction pathways. The OH-initiated pathway is represented by $Hg^{II}OHO$ reduction by CO. Simulated versus observed Δ^{200}Hg values for atmospheric Hg species when even-MIF occurs in: (**G**) Hg^{II}(p) photoreduction (*E* = −0.8‰); (**H**) the OH-initiated chemical pathway (represented by $Hg^{II}OHO$ reduction by CO, *E* = −1.8‰); and (**I**) both Hg^{II}(p) photoreduction and OH-initiated chemical pathway. Black diagonal lines denote 1:1 agreement.

inducing even-MIF, future experimental measurements or detailed chemical calculations are required. Nonetheless, this phenomenon enables us to represent the entire OH-initiated pathway by applying even-MIF to a selected process in subsequent analyses.

The correlation coefficients analysis identifies three potential processes capable of reproducing the global distribution trends of observed Δ^{200}Hg data: (i) Hg^{II}(p) photoreduction, (ii) OH-initiated reactions, and (iii) a combination of both (Fig. 2F). To evaluate these possibilities within the constraints of global observations, we tested the three processes using various enrichment factors. As shown in Fig. 2 (G to I), the optimal simulated results were obtained at *E* = −0.8‰ for Hg^{II}(p) photoreduction, *E* = −1.8‰ for OH-initiated pathway, and *E* = −0.5‰ for the combined process [involving both Hg^{II}(p) photoreduction and OH-initiated pathway]. A comparison of statistical metrics (table S1) indicates that the combined scenario (Fig. 2I) shows a "best case" and aligns more closely with observations. Specifically, three simulations yielded mean Δ^{200}Hg values comparable to observed data, but the combined scenario produced the lowest root mean square error (RMSE = 0.06) and a high correlation coefficient ($r = 0.65$, $P < 0.01$) for $\Delta^{200}Hg^{II}$(p, g), consistent with values observed at remote mountain sites (~0.10‰) and in near-shore and marine boundary layer environments (~0.05‰). Notably, the combined scenario also yielded the lowest RMSE (0.02) and highest correlation ($r = 0.79$, $P < 0.01$) for $\Delta^{200}Hg^{II}$(pre), outperforming the Hg^{II}(p) photoreduction (RMSE = 0.03, $r = 0.68$, $P < 0.01$) and OH-initiated pathway (RMSE = 0.05, $r = 0.61$, $P < 0.01$) scenarios (Fig. 2, G and I, and table S1). These findings suggest that, based on the latest atmospheric Hg chemical mechanisms (*29*), OH-initiated chemistry and Hg^{II}(p) photoreduction likely play a dominant role in driving atmospheric even-MIF.

Global distribution of even-MIF

Our model simulates the global distribution of even-MIF in the atmosphere (Figs. 3 and 4). Based on the best case simulation, the model simulates global $\Delta^{200}Hg^0$ values in surface atmosphere ranging from −0.09 to −0.04‰, with higher in the Southern Hemisphere (mean: −0.05 ± 0.01‰) compared to the Northern Hemisphere (mean: −0.07 ± 0.01‰). Observations are generally sparse and primarily clustered in heavily populated regions of the Northern Hemisphere (e.g., East Asia and North America) (Fig. 3A). The modeled $\Delta^{200}Hg^0$ is generally comparable with observations, with global mean of −0.06 ± 0.01‰ and −0.05 ± 0.03‰ ($n = 69$), respectively. The model successfully reproduces the gradient of observed $\Delta^{200}Hg^0$ that shows higher values in East Asia (model mean: −0.06 ± 0.01‰; observation mean: −0.03 ± 0.03‰, $n = 25$) than in North America (model mean: −0.07 ± 0.01‰; observation mean: −0.07 ± 0.02‰, $n = 39$). It also suggests that the global distribution pattern of $\Delta^{200}Hg^0$ is influenced by both emission sources and chemical isotopic fractionation. Despite higher photolysis rates of $Hg^{II}(p)$ in East Asia (0.08 ± 0.09 Mg year^{-1}) compared to North America (0.01 ± 0.01 Mg year^{-1}) (fig. S9A), chemical fractionation has a lower impact in East Asia. This is due to notably higher anthropogenic Hg emissions in East Asia (~1000 Mg year^{-1}) compared to North America (~50 Mg year^{-1}) (fig. S10A) (*34*), causing the $\Delta^{200}Hg^0$ signatures in East Asia to primarily reflect near-zero of anthropogenic emissions (Table 1), while $\Delta^{200}Hg^0$ signatures in North America are more influenced by chemical effects and tend to be more negative. Thus, $\Delta^{200}Hg^0$ signatures in regions with low anthropogenic emissions are more affected by chemical fractionation. In addition, the modeled $\Delta^{200}Hg^0$ values over land are generally lower than those over the ocean. The lower $\Delta^{200}Hg^0$ values can be transported to the oceanic atmosphere by wind (fig. S10B), particularly affecting $\Delta^{200}Hg^0$ values over the Northern Hemisphere oceans. In the Southern Hemisphere, redox chemical rates are minimal, especially between 60°S and 80°S (fig. S9, A and B), resulting in $\Delta^{200}Hg^0$ signatures influenced primarily by oceanic emissions (0.04 ± 0.02‰), which are higher than in other regions. These findings indicate that while atmospheric $\Delta^{200}Hg^0$ is a reliable tracer, emission sources and chemical fractionation contribute to potential spatial variations. Therefore, regional atmospheric $\Delta^{200}Hg^0$ characteristics must be considered when applying this tracer to regional mercury cycling.

Compared with $\Delta^{200}Hg^0$, the simulated $\Delta^{200}Hg^{II}(p)$ show opposite distribution pattern (Fig. 3B), indicating distinct chemical fractionation processes for even-MIF in atmospheric Hg. The modeled $\Delta^{200}Hg^{II}(p)$ values are predominantly positive across most land regions, with a mean of 0.08 ± 0.10‰ over land and 0.01 ± 0.04‰ over the ocean. Regions experiencing net oxidation of atmospheric Hg, such as partly of the central Pacific and Indian Oceans and the high-latitude Southern Hemisphere (60°S to 80°S) (fig. S10C), show negative $\Delta^{200}Hg^{II}(p)$ values. The simulated $\Delta^{200}Hg^{II}(p)$ align well with observations in both remote mountains, urban, and near-shore environment areas, with modeled values of 0.11 ± 0.07‰ ($n = 4$), 0.06 ± 0.05‰ ($n = 14$), and 0.04 ± 0.06‰ ($n = 6$) compared to observed values of 0.10 ± 0.03‰ ($n = 4$) (*10*, *35*),

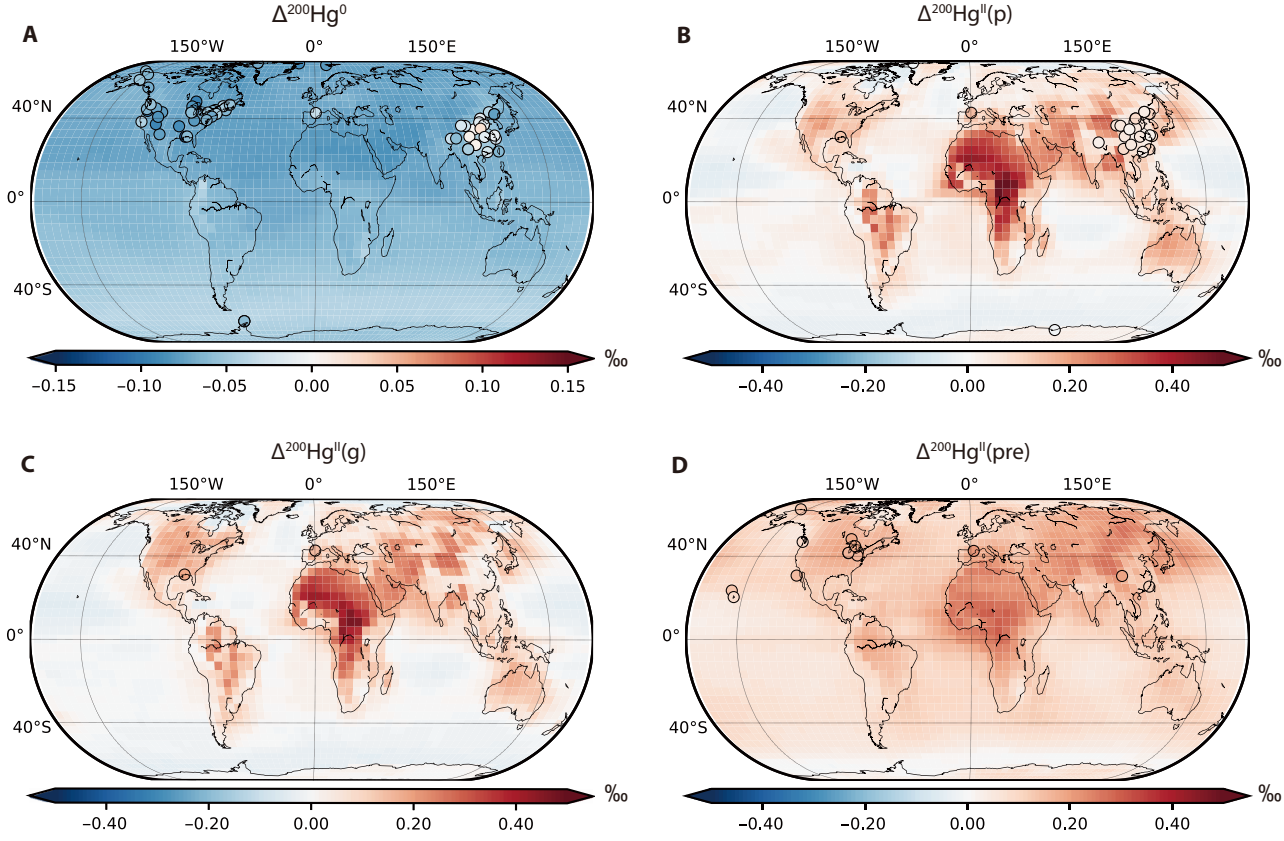

Fig. 3. Results comparison of simulated (annual mean) $\Delta^{200}Hg$ and available observations (indicated as points) in the surface atmosphere. (**A**) $\Delta^{200}Hg^0$, (**B**) $\Delta^{200}Hg^{II}(p)$, (**C**) $\Delta^{200}Hg^{II}(g)$, and (**D**) $\Delta^{200}Hg^{II}(pre)$. All observations are synthesized from publications, as detailed in fig. S1.

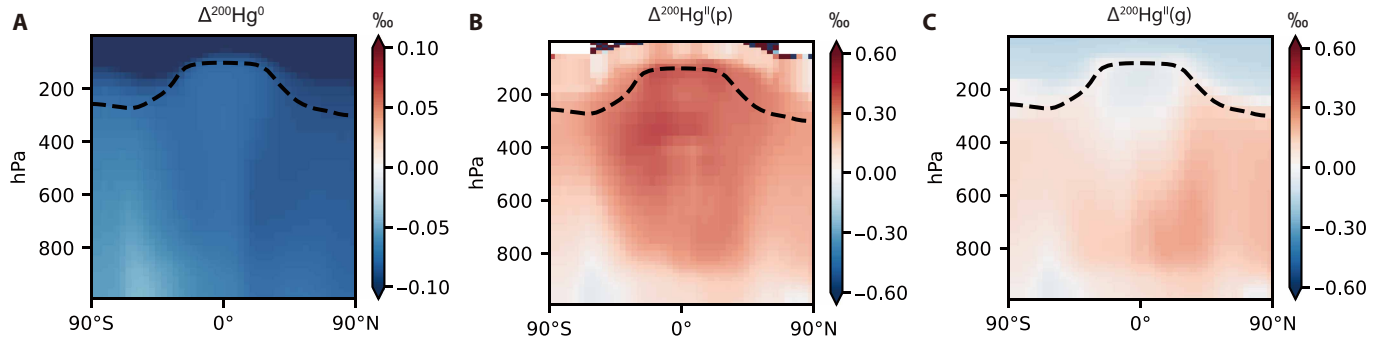

Fig. 4. Distribution of the simulated zonal annual mean across the global atmosphere. (**A**) $\Delta^{200}Hg^{0}$, (**B**) $\Delta^{200}Hg^{II}$(p), and (**C**) $\Delta^{200}Hg^{II}$(g). The dashed lines denote the annual-mean tropopause.

0.05 ± 0.02‰ (n = 14) (*16*, *36*–*39*), and 0.05 ± 0.06‰ (n = 6) (*13*, *40*–*44*), respectively (Fig. 3B). The simulated high $\Delta^{200}Hg^{II}$(p) values over land regions, such as Africa, North and South America, and Australia are also potentially influenced by Hg transportation from high-altitude free troposphere. In urban sites in East Asia, $\Delta^{200}Hg^{II}$(p) signatures are primarily shaped by anthropogenic emissions, similar to the $\Delta^{200}Hg^{0}$ signatures discussed previously. Our model also highlights notable variation in $\Delta^{200}Hg^{II}$(p) signatures within the marine boundary layer. Given the relatively low chemical rates of OH-initiated oxidation and Hg^{II}(p) photolysis in the marine boundary layer (figs. S9, C and D and S10D), the positive Hg^{II}(p) signatures in these regions mainly originate from land and free troposphere.

The simulated $\Delta^{200}Hg^{II}$(g) signatures in surface atmosphere show comparable values and patterns to $\Delta^{200}Hg^{II}$(p) in both terrestrial and marine atmospheres (Fig. 3C) due to the adsorption and desorption of Hg^{II}(g) on particulate-bound Hg (*29*). The modeled $\Delta^{200}Hg^{II}$(pre) values show a distribution pattern comparable to $\Delta^{200}Hg^{II}$(g) and $\Delta^{200}Hg^{II}$(p), as precipitation removes Hg from both Hg^{II}(p) and Hg^{II}(g), leading to higher $\Delta^{200}Hg^{II}$(pre) values over land (0.13 ± 0.06‰) compared to the ocean (0.08 ± 0.04‰) (Fig. 3D). Our model simulates consistent $\Delta^{200}Hg^{II}$(pre) values with observations (0.15 ± 0.04‰, n = 15) (*14*, *15*, *45*–*53*), except for the observation at Peterborough, Canada (*12*, *54*). The model underestimates the mean $\Delta^{200}Hg^{II}$(pre) (~0.16‰) compared to observations (~0.30 to 0.40‰) at Peterborough (*12*, *54*). This discrepancy may arise from the absence of UV irradiation–induced fractionation in our model, which is hypothesized to occur via lightning (*21*) or in the stratosphere (*33*). This fractionation may potentially influence isotopic signatures in precipitation during droplets formation, in-cloud, or aqueous-phase chemistry processes. Another potential source of bias could be the model resolution; the 4° by 5° GEOS-Chem model may not adequately capture high-altitude precipitation events in North America (*55*), thereby underestimating the elution of Hg with positive $\Delta^{200}Hg^{II}$ values from higher altitudes.

Vertical distributions of $\Delta^{200}Hg$ in various atmospheric Hg species also exhibit distinct patterns (Fig. 4). The simulated zonal mean $\Delta^{200}Hg^{0}$ generally shows negative values (global zonal mean: −0.09 ± 0.02‰). Elevated $\Delta^{200}Hg^{0}$ values in the Southern Hemisphere are influenced by oceanic emissions, which contribute higher $\Delta^{200}Hg^{0}$ signatures to the upper atmosphere in this region (Fig. 4A). In contrast, $\Delta^{200}Hg^{II}$(p) displays predominantly positive values (global zonal mean: 0.18 ± 0.11‰) (Fig. 4B). Notably, $\Delta^{200}Hg^{II}$(p) reaches up to 0.5‰ in the free troposphere (<800 hPa), driven by enhanced redox activity in this region (fig. S9). This may explain why high-altitude mountain sites (*10*, *35*) typically record higher $\Delta^{200}Hg^{II}$(p) values than urban areas (*16*, *36*–*39*) and near-shore environment (*13*, *40*–*44*). While surface values and trends are similar, the zonal distribution of $\Delta^{200}Hg^{II}$(g) (global zonal mean: 0.02 ± 0.11‰) differs markedly from that of $\Delta^{200}Hg^{II}$(g) (Fig. 4C). This divergence arises because $\Delta^{200}Hg^{II}$(g) in the free troposphere is strongly influenced by OH-initiated oxidation, which produces $Hg^{II}(OH)_2$—the dominant gaseous Hg^{II} species that does not photolyze (fig. S8)— and carries relatively low $\Delta^{200}Hg$ values in the tropical upper troposphere (<400 hPa). In addition, both Hg^{II}(p) and Hg^{II}(g) exhibit relatively lower $\Delta^{200}Hg$ values in the lower atmosphere (>800 hPa), as Hg^{II} in this area is predominantly formed via the Br-initiated pathway, which does not induce even-MIF (fig. S8). These results help explain why precipitation typically exhibits higher $\Delta^{200}Hg$ values than Hg^{II}(p, g) in observational measurements. As most precipitation originates in the free troposphere (fig. S8A), it efficiently scavenges Hg^{II}(g) and Hg^{II}(p) carrying notable positive $\Delta^{200}Hg$ values (fig. S8, B to G).

DISCUSSION

Implications

Our modeling represents an optimal simulation scenario; however, further experimental verification is necessary to confirm the specific mechanisms underlying even-MIF. Although our results suggest that Hg^{II}(p) photoreduction may contribute to even-MIF—supporting recent hypotheses that a molecular magnetic isotope effect during Hg^{II} photoreduction on aerosols containing magnetic halogen nuclei could induce even-MIF (*10*)—recent experimental studies on Hg^{II} photoreduction on soot particles (*56*) and in aqueous organic ligands (*10*, *57*–*59*) did not detect even-MIF. We speculate that this discrepancy may stem from differences in aerosol type and the surface photochemical processes occurring in heterogeneous environments, in line with recent proposals (*12*, *17*). Based on the "best case" simulation, we additionally imposed odd-MIF only during the photoreduction of Hg^{II}(p) (see Materials and Methods), and the resulting $\Delta^{199}Hg/\Delta^{200}Hg$ patterns partially reproduced observational data (fig. S11). This outcome provides further support for the possibility that Hg^{II}(p) photoreduction, a key source of atmospheric odd-MIF (*31*, *60*), may also contribute to the formation of $\Delta^{200}Hg$. Moreover, there is currently no computational or experimental evidence linking OH-initiated chemical processes with even-MIF. As the OH-initiated pathway accounts for roughly half of the net oxidation of Hg^{0} to Hg^{II} (*29*), assigning even-MIF to this pathway is, to some extent, functionally equivalent to attributing it to Hg^{II}(p) photoreduction. Our model cannot differentiate between these two mechanisms. Therefore, we call for additional computational and experimental

studies focusing on the atmospheric chemical processes involving various types of particulate organic matter and OH radicals.

Our model reveals substantial variations in Δ^{200}Hg signatures in the atmosphere, particularly for Hg^{II}(g), Hg^{II}(p), and Hg^{II}(pre) (table S2), highlighting the importance of considering spatial heterogeneity when using Δ^{200}Hg to trace Hg sources. For example, the simulated mean values of $\Delta^{200}Hg^{II}$(g) (0.25 ± 0.10‰) and $\Delta^{200}Hg^{II}$(p) (0.27 ± 0.11‰) over the African continent are notably higher compared to other continents. There are also notable differences in the mean values of Δ^{200}Hg for Hg^{II}(p, g) and wet deposition in the atmosphere over land and ocean (range of differences: 0.00 to 0.13‰). This highlights the necessity of analyzing local atmospheric end-member Hg isotope signatures in parallel to avoid bias when evaluating Hg sources and processes, particularly in land, coastal, and open-ocean environments. These variations also help explain why the box isotopic model can reproduce the observed relative Δ^{200}Hg values between Hg^0 and Hg^{II} but not the absolute $\Delta^{200}Hg^0$ and $\Delta^{200}Hg^{II}$ (*60*), as the box model cannot take into account spatial heterogeneity, and the spatial inhomogeneity of redox chemistry determines the spatial distribution of even-MIF.

Moreover, the model suggests substantial differences in the isotopic signatures of various Hg species, indicating the need for future research to develop isotopic measurements specific to Hg species for tracing the transport and transformation of atmospheric Hg. Meanwhile, given the ease with which Hg^{II}(g) and Hg^{II}(p) are removed, we recommend that dry deposition of atmospheric Hg^{II} be considered when assessing atmospheric sources to Earth's surface. Future observational studies should focus on methods for collecting and analyzing isotopic signatures from atmospheric Hg dry deposition. In addition, our results indicate that Hg emissions from anthropogenic sources can affect Δ^{200}Hg signatures of atmospheric Hg (e.g., in East Asia and South America; Fig. 3 and table S2). These findings imply that Δ^{200}Hg should be used with caution to identify potential sources and calls for more observations and further research to clarify the underlying influence factors.

MATERIALS AND METHODS

Atmospheric Hg model

We use the GEOS-Chem model (version 12.9.0) with a resolution of 4°latitude by 5° longitude and 47 vertical layers (*31*, *32*). The model uses the native MERRA2 (4° by 5°) reanalysis meteorological data. Anthropogenic Hg emissions are derived from Streets *et al.* (*34*), and all the natural emissions are cited from Shah *et al.* (*29*). The model incorporates dynamic coupling between atmosphere and earth surface using gridded land and ocean surface Hg concentrations as boundary conditions (*29*, *30*). The dry deposition velocity for Hg^0 over land is calculated using a resistance-in-series scheme (*61*). Over the ocean, the Hg^0 uptake is controlled by the air-sea exchange model (*62*). Dry deposition velocity for the atmospheric Hg^{II}(g) is biologically unreactive and has a highly high Henry's law constant. Dry deposition of Hg^{II}(p) is calculated according to the aerosol deposition scheme (*62*, *63*). The model also simulates wet scavenging of Hg^{II} [sum of Hg^{II}(g) and Hg^{II}(p)] following the scheme proposed by Amos *et al.* (*64*) and Liu *et al.* (*65*).

This model incorporates the latest advancement in the atmospheric Hg chemistry mechanism (*29*), wherein Br and OH contribute comparably to global net Hg^0 oxidation to Hg^{II} (Fig. 5). Intermediate products of $Hg^{I}Br$ and $Hg^{I}OH$ can be further oxidized to Hg^{II} by ozone and radicals. Atmospheric Hg^{II} can be speciated in aerosols and could droplets, and both gaseous and heterogeneous Hg^{II} can be reduced back to Hg^0 (*29*). Hg^{II}(p) in the tropospheric aerosol can be divided into Hg^{II}-organic and Hg^{II}-inorganic complexes, which are speciated according to local mass fraction of organic aerosols in fine particles (*29*). Overall, the chemistry mechanism mainly contains four redox pathways, namely, Br-initiated redox reactions, Cl-initiated redox reactions, OH-initiated redox reactions, and Hg^{II}(p) photolysis on organic aerosol.

Hg isotope model

The three-dimensional atmospheric Hg isotope model is developed on the basis of the GEOS-Chem platform as described above. All the seven stable isotopes (^{196}Hg, ^{198}Hg, ^{199}Hg, ^{200}Hg, ^{201}Hg, ^{202}Hg, and ^{204}Hg) are integrated as independent traces, resulting in 175 advected tracers in the model. The redox chemistry processes are solved using kinetic preprocessor customized for GEOS-Chem (*66*, *67*). The isotopes have consistent chemical and physical processes but different chemistry rates for processes that induce isotopic fractionation. Both the anthropogenic and natural Hg emissions are contained, and the corresponding isotopic signatures are also integrated as displaying in Table 1. The model simulation spans from 2016 to 2018. By initializing the model with the first 2 years, the third year is used for result analysis.

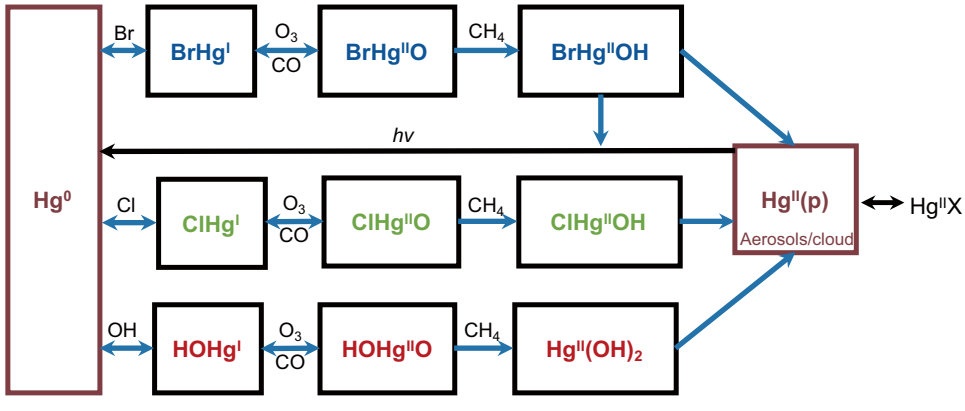

Fig. 5. The four major atmospheric Hg redox pathways in the GEOS-Chem model. The chemistry mechanism is from Shah *et al.* (*29*) (https://pubs.acs.org/doi/10.1021/acs.est.1c03160; https://creativecommons.org/licenses/by-nc-nd/4.0/).

We use the same notation as suggested by Blum and Bergquist (*68*) to express the simulated isotope composition. The notations are defined as isotope ratio difference between simulated species and the NIST-3133 standard in a unit of permil (‰)

$$\delta^{xxx}\mathrm{Hg}\,(‰) = \left[\left({}^{xxx/198}\mathrm{Hg}/{}^{xxx/198}\mathrm{Hg}_{NIST3133}\right) - 1\right] \times 1000 \quad (1)$$

MIF is calcuated as below

$$\Delta^{199}\mathrm{Hg} = \delta^{199}\mathrm{Hg} - \delta^{202}\mathrm{Hg} \times 0.252 \quad (2)$$

$$\Delta^{200}\mathrm{Hg} = \delta^{200}\mathrm{Hg} - \delta^{202}\mathrm{Hg} \times 0.502 \quad (3)$$

$$\Delta^{201}\mathrm{Hg} = \delta^{201}\mathrm{Hg} - \delta^{202}\mathrm{Hg} \times 0.752 \quad (4)$$

$$\Delta^{204}\mathrm{Hg} = \delta^{204}\mathrm{Hg} - \delta^{202}\mathrm{Hg} \times 1.493 \quad (5)$$

The ${}^{xxx/198}Hg_{NIST3133}$ ratios in Eq. 1 are treated as constants, which are calculated from Hg atomic abundances in NIST-3133 standard (*68*, *69*), namely, ^{196}Hg = 0.155%, ^{198}Hg = 10.04%, ^{199}Hg = 16.94%, ^{200}Hg = 23.14%, ^{201}Hg = 13.17%, ^{202}Hg = 29.73%, and ^{204}Hg = 6.83%. We synthesize the Hg isotope composition (δ and Δ) of each source and calculate its isotope ratio ($^{xxx/198}$Hg) using Eqs.1 to 5. The isotope ratios can divide the total Hg emissions into seven isotopes that can be input into the model. After running, we can calculate the isotope composition also by using Eqs. 1 to 5.

Isotope fractionation in the model is treated as kinetic processes. We slightly perturb the reaction rates of various isotopes to make differences of the transformation of the isotope during chemical processes. The rules for this perturbation strictly follow the theory of MDF and MIF calculations for Hg isotopes. ^{198}Hg is treated as the base isotope that contains the chemistry rates (K_{198}) same as the standard GEOS-Chem. The K_{xxx} for other six isotope is calculated as follows

$$K_{xxx} = K_{198} \times \alpha^{xxx/198}\mathrm{Hg}_{tot} \quad (6)$$

where the process-based kinetic fractionation factors ($\alpha^{xxx/198}Hg_{tot}$) are defined as the ratio of $^{xxx/198}$Hg for the product over reactant, including two parts: $\alpha^{xxx/198}Hg_{MDF}$ and $\alpha^{xxx/198}Hg_{MIF}$. The reported $\alpha^{xxx/198}Hg_{MDF}$ obey the MDF kinetic laws during Hg transfer (*8*, *25*)

$$\ln\left(\alpha^{xxx/198}\mathrm{Hg}_{MDF}\right) = \beta_{xxx} \times \ln\left(\alpha^{202/198}\mathrm{Hg}\right) \quad (7)$$

The β is taken as −0.507, 0.252, 0.502, 0.752, and 1.493 for ^{196}Hg, ^{199}Hg, ^{200}Hg, ^{201}Hg, ^{202}Hg, and ^{204}Hg, respectively. Previous studies have reported Hg isotope enrichment factors (ε^{xxx}Hg for MDF and E^{xxx}Hg for MIF) during many physical and chemical processes, which are calculated from the difference in the MDF and MIF signature as product over reactant Hg pools (*60*). Process-based kinetic fractionation factors ($\alpha^{xxx/198}$Hg) can be calculated as follows

$$\ln\left(\alpha^{xxx/198}\mathrm{Hg}_{MDF}\right) = \varepsilon^{xxx}\mathrm{Hg}/1000 \quad (8)$$

$$\ln\left(\alpha^{xxx/198}\mathrm{Hg}_{MIF}\right) = E^{xxx}\mathrm{Hg}/1000 \quad (9)$$

The $\alpha^{xxx/198}Hg_{tot}$ is calculated as follows

$$\alpha^{xxx/198}\mathrm{Hg}_{tot} = \alpha^{xxx/198}\mathrm{Hg}_{MDF} \times \alpha^{xxx/198}\mathrm{Hg}_{MIF} \quad (10)$$

In this study, we applied the MIF effects to both ^{199}Hg, ^{200}Hg, and ^{204}Hg isotopes, and we mainly focus on the modeled Δ^{200}Hg values for atmospheric Hg^0, Hg^{II}(p, g), and precipitation, with the modeled Δ^{199}Hg and Δ^{204}Hg values are discussed and presented in the Supplementary Materials. The fractionation factors can relatively perturb the chemistry rates of ^{199}Hg, ^{200}Hg, and ^{204}Hg, allowing the model to replicate a fractionation effect similar to that observed in the atmosphere, wherein the Hg^{II} enriches odd-Hg and even-Hg isotopes. We excluded discussing the MDF, as it is affected by almost all the physical and chemical process (*8*, *70*). The simulation of odd-MIF is similar with our previous study (*31*). Odd-MIF was exclusively applied to the photolysis of Hg^{II}(p) process, which can be interpreted as MIF brought on by Hg^{II}(p) photoreduction. The E^{199}Hg for Hg^{II}(p) photolysis was estimated at −2.75 ± 0.14‰ (*60*, *71*). However, in this study, we used E^{199}Hg of −2.25‰, which more accurately reproduces Δ^{199}Hg signatures in atmospheric Hg. In addition, we modeled Δ^{204}Hg based on source emissions and enrichment factors derived from the empirical relationship $\Delta^{200}Hg/\Delta^{204}Hg = -0.5‰$, as observed in natural samples (*70*).

Synthesized observation datasets

We synthesized observed Δ^{200}Hg data from global atmospheric samples, including gaseous, particulate, and precipitation samples, as shown in fig. S1. $\Delta^{200}Hg^0$ observations are primarily located in East Asia and North America, with a global mean of −0.05 ± 0.03‰ (n = 69). The $\Delta^{200}Hg^0$ in East Asia is ~−0.03 ± 0.03‰, a little higher than in North America of −0.07 ± 0.02‰. The $\Delta^{200}Hg^{II}$(p) data include observations from land remote mountain sites (n = 4), urban sites (n = 14), and marine boundary layer and near-shore environment (MBL and near-shore, n = 6). The remote mountain sites show higher $\Delta^{200}Hg^{II}$(p) than MBL and near-shore areas, with means of 0.10 ± 0.03 and 0.05 ± 0.06‰, respectively. Two $\Delta^{200}Hg^{II}$(g) data have collected from Grand Bay, USA (0.18 ± 0.07‰) (*13*) and Pic du Midi, France (0.15 ± 0.06‰) (*10*). Precipitations samples are also primarily located in East Asia and North America, with a global mean of 0.15 ± 0.04‰ (n = 15). Overall, the data indicate that precipitation samples exhibit the highest levels of even-MIF fractionation, followed by Hg^{II}(p) and then Hg^0. These datasets include all observed raw data from each site, averaged across the sites, and were used to validate the model's simulation results.

Uncertainty

The uncertainties in our model primarily arise from the Hg isotope signatures of source emissions. As shown in Table 1, the Δ^{200}Hg of GEM emissions has standard deviations ranging from 0.02 to 0.05‰. To assess the impact of the upper and lower limits (maximum or minimum isotopic composition) of different emission sources on the modeling results, we conducted sensitivity simulations. The results indicate that the uncertainties in source emissions can lead to shifts of ±0.02 to ±0.03‰ in the simulated $\Delta^{200}Hg^0$, $\Delta^{200}Hg^{II}$(g), $\Delta^{200}Hg^{II}$(p), and $\Delta^{200}Hg^{II}$(pre) (fig. S12), which has minimal impact on the analysis of these Δ^{200}Hg values.

Another source of uncertainty arises from the chemical kinetic rate constants governing atmospheric Hg. Although our model incorporates recent advances in atmospheric Hg chemistry, several processes remain uncertain and may influence the results. For example, the photoreduction rate of Hg^{II}(p) has not been experimentally determined, and the reduction rate constant in our model is based on the photolysis rate of NO_2, scaled to match global atmospheric Hg concentrations. Furthermore, the model does not account

for the influence of anthropogenic short-lived halogens on atmospheric Hg (*72*). To assess the impact of these uncertainties, we conducted sensitivity tests by perturbing all chemical rates by −50 and +150%, respectively. As shown in fig. S13A, the modeled $\Delta^{200}Hg^0$ is most sensitive to changes in the kinetic rate constants, followed by $\Delta^{200}Hg^{II}$(p) and then $\Delta^{200}Hg^{II}$(pre). Given that the $\Delta^{200}Hg^0$ values are much lower, the uncertainty in the chemical rates has a relatively minor impact on $\Delta^{200}Hg^0$ values. However, when sensitivity tests were applied only to even-MIF–associated chemical rates, the changes in $\Delta^{200}Hg^{II}$(p) and $\Delta^{200}Hg^{II}$(pre) were substantially larger than those in $\Delta^{200}Hg^0$ (fig. S13B), suggesting that uncertainties in the OH-initiated chemical and the Hg^{II}(p) photoreduction rates notably affect the simulation outcomes. While uncertainties in chemical rates alter the magnitude of the simulation results, they have little effect on their spatial distribution, as evidenced by a strong positive correlation between the simulation outputs before and after the chemical rate changes (fig. S13, C and D).

Uncertainties in enrichment factors also contribute to variability in the modeling outcomes. We considered uncertainties of 50 and 100% and scaled the enrichment factors based on the "best case" simulation. As shown in fig. S13E, when the enrichment factor changes by 50 and 100%, the simulated $\Delta^{200}Hg^0$ is most sensitive, with changes of 59 and 100%, respectively. In contrast, the modeled $\Delta^{200}Hg^{II}$(pre) and $\Delta^{200}Hg^{II}$(p, g) exhibit changes of 49 and 96% and 38 and 88%, respectively. As the enrichment factor increases, the gap between $\Delta^{200}Hg^{II}$ and $\Delta^{200}Hg^0$ widens, with $\Delta^{200}Hg^{II}$ shifting positively and $\Delta^{200}Hg^0$ negatively (fig. S13F). Notably, $\Delta^{200}Hg$ in precipitation shows the largest variation, while $\Delta^{200}Hg$ in Hg^{II}(p, g) and Hg^0 exhibit comparable variations. In addition, in our "best case" scenario, we applied the same enrichment factor ($E = -0.5‰$) to both Hg^{II}(p) photoreduction and OH-initiated oxidation pathways. This value is not intended to reflect actual environmental conditions, as similar simulation outcomes could theoretically be achieved using different enrichment factors for each process. Determining the true values of the enrichment factors will require validation through future experimental studies.

Moreover, our modeling results are limited by the simplified stratospheric Hg redox chemistry, which has been evaluated in recent studies (*33*, *73*). Environmental conditions in the stratosphere—such as intense UV radiation, high ozone concentrations, and lower atmospheric pressure—differ notably from those in the troposphere and could potentially affect even-MIF. Although our model does not incorporate the most recent advances in stratospheric chemistry mechanisms, which include 60 reactions (*33*), this mechanism still involves the three oxidation pathways—Br reactions, Cl reactions, and OH reactions. In addition, as the $\Delta^{200}Hg$ signal can propagate within the same pathway, we speculate that the modeling results based on stratospheric chemistry (*33*) should show similarities to our experiments. Although Sun *et al.* (*21*) reported negligible even-MIF in $Hg + O_3 + N_2$ reaction mixtures, we advocate for further observational, experimental, and modeling studies to investigate stratospheric even-MIF patterns.

Supplementary Materials

The PDF file includes:

Text S1 and S2
Figs. S1 to S14
Tables S1 and S2
Legend for data S1
References

Other Supplementary Material for this manuscript includes the following:

Data S1

REFERENCES AND NOTES

1. Y. Zhang, Z. Song, S. Huang, P. Zhang, Y. Peng, P. Wu, J. Gu, S. Dutkiewicz, H. Zhang, S. Wu, F. Wang, L. Chen, S. Wang, P. Li, Global health effects of future atmospheric mercury emissions. *Nat. Commun.* **12**, 3035 (2021).
2. R. Sun, H. Hintelmann, J. A. Wiklund, M. S. Evans, D. Muir, J. L. Kirk, Mercury isotope variations in lake sediment cores in response to direct mercury emissions from non-ferrous metal smelters and legacy mercury remobilization. *Environ. Sci. Tech.* **56**, 8266–8277 (2022).
3. H. M. Amos, D. J. Jacob, D. G. Streets, E. M. Sunderland, Legacy impacts of all-time anthropogenic emissions on the global mercury cycle. *Global Biogeochem. Cycles* **27**, 410–421 (2013).
4. D. Obrist, J. L. Kirk, L. Zhang, E. M. Sunderland, M. Jiskra, N. E. Selin, A review of global environmental mercury processes in response to human and natural perturbations: Changes of emissions, climate, and land use. *Ambio* **47**, 116–140 (2018).
5. M. Jiskra, L.-E. Heimbürger-Boavida, M.-M. Desgranges, M. V. Petrova, A. Dufour, B. Ferreira-Araujo, J. Masbou, J. Chmeleff, M. Thyssen, D. Point, J. E. Sonke, Mercury stable isotopes constrain atmospheric sources to the ocean. *Nature* **597**, 678–682 (2021).
6. R. Zhang, R. Sun, Y. Liu, S. Li, F. Cao, H. Yang, S. Chen, X. Li, W. Zheng, J. Chen, Mercury isotope composition in open water corals of South China Sea: Implication for atmospheric mercury deposition pathways into tropical oceans. *Geophys. Res. Lett.* **50**, e2023GL105305 (2023).
7. C. Li, M. Jiskra, M. B. Nilsson, S. Osterwalder, W. Zhu, D. Mauquoy, U. Skyllberg, M. Enrico, H. Peng, Y. Song, E. Björn, K. Bishop, Mercury deposition and redox transformation processes in peatland constrained by mercury stable isotopes. *Nat. Commun.* **14**, 7389 (2023).
8. B. A. Bergquist, Mercury Isotopes, in *Encyclopedia of Engineering Geology Encyclopedia of Earth Sciences Series*, W. White, Ed. (Springer, Cham., 2018), pp. 1–7.
9. J. D. Blum, L. S. Sherman, M. W. Johnson, Mercury isotopes in Earth and environmental sciences. *Annu. Rev. Earth Planet. Sci.* **42**, 249–269 (2014).
10. X. Fu, M. Jiskra, X. Yang, N. Marusczak, M. Enrico, J. Chmeleff, L. E. Heimburger-Boavida, F. Gheusi, J. E. Sonke, Mass-independent fractionation of even and odd mercury isotopes during atmospheric mercury redox reactions. *Environ. Sci. Tech.* **55**, 10164–10174 (2021).
11. H. M. Cai, J. B. Chen, Mass-independent fractionation of even mercury isotopes. *Sci. Bull.* **61**, 116 (2016).
12. J. B. Chen, H. Hintelmann, X. B. Feng, B. Dimock, Unusual fractionation of both odd and even mercury isotopes in precipitation from Peterborough, ON, Canada. *Geochim. Cosmochim. Acta* **90**, 33 (2012).
13. J. M. Rolison, W. M. Landing, W. Luke, M. Cohen, V. J. M. Salters, Isotopic composition of species-specific atmospheric Hg in a coastal environment. *Chem. Geol.* **336**, 37–49 (2013).
14. J. D. Demers, J. D. Blum, D. R. Zak, Mercury isotopes in a forested ecosystem: Implications for air-surface exchange dynamics and the global mercury cycle. *Global Biogeochem. Cycles* **27**, 222–238 (2013).
15. L. E. Gratz, G. J. Keeler, J. D. Blum, L. S. Sherman, Isotopic composition and fractionation of mercury in Great Lakes precipitation and ambient air. *Environ. Sci. Tech.* **44**, 7764–7770 (2010).
16. C. Liu, X. Fu, Y. Xu, H. Zhang, X. Wu, J. Sommar, L. Zhang, X. Wang, X. Feng, Sources and transformation mechanisms of atmospheric particulate bound mercury revealed by mercury stable isotopes. *Environ. Sci. Tech.* **56**, 5224–5233 (2022).
17. D. AuYang, J. Chen, W. Zheng, Y. Zhang, G. Shi, J. E. Sonke, P. Cartigny, H. Cai, W. Yuan, L. Liu, P. Gai, C. Liu, South-hemispheric marine aerosol Hg and S isotope compositions reveal different oxidation pathways. *Natl Sci. Open* **1**, 20220014 (2022).
18. Y. Qiu, P. X. Gai, F. E. Yue, Y. Y. Zhang, P. Z. He, H. Kang, X. W. Yu, P. K. S. Lam, J. B. Chen, Z. Q. Xie, Identification of potential sources of elevated PM2.5-Hg using mercury isotopes during haze events. *Atmos. Environ.* **247**, 118203 (2021).
19. Y. Qiu, P. Gai, F. Yue, Y. Zhang, P. He, H. Kang, X. Yu, P. K. S. Lam, J. Chen, Z. Xie, Stable mercury isotopes revealing photochemical processes in the marine boundary layer. *J. Geophys. Res. Atmos.* **126**, e2021JD034630 (2021).
20. S. Huang, Y. Huo, H. Sun, S. Lv, Y. Zhao, K. Lin, Y. Chen, Y. Zhang, Evidence for mass independent fractionation of even mercury isotopes in the troposphere. *Atmos. Chem. Phys. Discuss.* **2022**, 1 (2022).
21. G. Sun, X. Feng, R. Yin, F. Wang, C. J. Lin, K. Li, J. O. Sommar, Dissociation of mercuric oxides drives anomalous isotope fractionation during net photo-oxidation of mercury vapor in air. *Environ. Sci. Tech.* **56**, 13428–13438 (2022).
22. G. Sun, J. Sommar, X. Feng, C. J. Lin, M. Ge, W. Wang, R. Yin, X. Fu, L. Shang, Mass-dependent and -independent fractionation of mercury isotope during gas-phase oxidation of elemental mercury vapor by atomic Cl and Br. *Environ. Sci. Tech.* **50**, 9232–9241 (2016).

23. S. Yang, Y. Liu, Nuclear volume effects in equilibrium stable isotope fractionations of mercury, thallium and lead. *Sci. Rep.* **5**, 12626 (2015).
24. E. A. Schauble, Role of nuclear volume in driving equilibrium stable isotope fractionation of mercury, thallium, and other very heavy elements. *Geochim. Cosmochim. Acta* **71**, 2170–2189 (2007).
25. B. A. Bergquist, J. D. Blum, Mass-dependent and -independent fractionation of Hg isotopes by photoreduction in aquatic systems. *Science* **318**, 417–420 (2007).
26. L. C. Motta, K. Kritee, J. D. Blum, M. T.-K. Tsui, J. R. Reinfelder, Mercury isotope fractionation during the photochemical reduction of Hg(II) coordinated with organic ligands. *J. Phys. Chem. A* **124**, 2842–2853 (2020).
27. L. C. Motta, A. D. Chien, A. E. Rask, P. M. Zimmerman, Mercury magnetic isotope effect: A plausible photochemical mechanism. *J. Phys. Chem. A* **124**, 3711–3719 (2020).
28. C. Mead, J. R. Lyons, T. M. Johnson, A. D. Anbar, Unique Hg stable isotope signatures of compact fluorescent lamp-sourced Hg. *Environ. Sci. Tech.* **47**, 2542–2547 (2013).
29. V. Shah, D. J. Jacob, C. P. Thackray, X. Wang, E. M. Sunderland, T. S. Dibble, A. Saiz-Lopez, I. Černušák, V. Kellö, P. J. Castro, R. Wu, C. Wang, Improved mechanistic model of the atmospheric redox chemistry of mercury. *Environ. Sci. Tech.* **55**, 14445–14456 (2021).
30. H. M. Horowitz, D. J. Jacob, Y. Zhang, T. S. Dibble, F. Slemr, H. M. Amos, J. A. Schmidt, E. S. Corbitt, E. A. Marais, E. M. Sunderland, A new mechanism for atmospheric mercury redox chemistry: Implications for the global mercury budget. *Atmos. Chem. Phys.* **17**, 6353–6371 (2017).
31. Z. Song, S. J. Huang, P. Zhang, T. F. Yuan, Y. X. Zhang, Isotope data constrains redox chemistry of atmospheric mercury. *Environ. Sci. Tech.* **58**, 13307–13317 (2024).
32. Z. Song, R. Sun, Y. Zhang, Modeling mercury isotopic fractionation in the atmosphere. *Environ. Pollut.* **307**, 119588 (2022).
33. A. Saiz-Lopez, C. A. Cuevas, A. U. Acuña, J. A. Añel, A. S. Mahajan, L. de la Torre, W. H. Feng, J. Z. Dávalos, D. Roca-Sanjuán, D. E. Kinnison, J. Carmona-García, R. P. Fernandez, Q. Y. Li, J. E. Sonke, A. Feinberg, J. C. G. Martín, J. Villamayor, P. Zhang, Y. X. Zhang, C. S. Blaszczak-Boxe, O. Travnikov, F. Y. Wang, J. Bieser, J. S. Francisco, J. M. C. Plane, Role of the stratosphere in the global mercury cycle. *Sci. Adv.* **11**, eads1459 (2025).
34. D. G. Streets, H. M. Horowitz, Z. Lu, L. Levin, C. P. Thackray, E. M. Sunderland, Global and regional trends in mercury emissions and concentrations, 2010–2015. *Atmos. Environ.* **201**, 417–427 (2019).
35. X. Fu, H. Zhang, X. Feng, Q. Tan, L. Ming, C. Liu, L. Zhang, Domestic and transboundary sources of atmospheric particulate bound mercury in remote areas of China: Evidence from mercury isotopes. *Environ. Sci. Tech.* **53**, 1947–1957 (2019).
36. J. Guo, C. M. Sharma, L. Tripathee, S. Kang, X. Fu, J. Huang, K. L. Shrestha, P. Chen, Source identification of atmospheric particle-bound mercury in the Himalayan foothills through non-isotopic and isotope analyses. *Environ. Pollut.* **286**, 117317 (2021).
37. H. M. Xu, R. Y. Sun, J. J. Cao, R.-J. Huang, B. Guinot, Z. X. Shen, M. Jiskra, C. X. Li, B. Y. Du, C. He, S. X. Liu, T. Zhang, J. E. Sonke, Mercury stable isotope compositions of Chinese urban fine particulates in winter haze days: Implications for Hg sources and transformations. *Chem. Geol.* **504**, 267–275 (2019).
38. H. Xu, J. E. Sonke, B. Guinot, X. Fu, R. Sun, A. Lanzanova, F. Candaudap, Z. Shen, J. Cao, Seasonal and annual variations in atmospheric Hg and Pb isotopes in Xi'an, China. *Environ. Sci. Tech.* **51**, 3759–3766 (2017).
39. Q. Huang, J. Chen, W. Huang, P. Fu, B. Guinot, X. Feng, L. Shang, Z. Wang, Z. Wang, S. Yuan, H. Cai, L. Wei, B. Yu, Isotopic composition for source identification of mercury in atmospheric fine particles. *Atmos. Chem. Phys.* **16**, 11773–11786 (2016).
40. W. Zheng, P. Chandan, A. Steffen, G. Stupple, J. De Vera, C. P. J. Mitchell, F. Wania, B. A. Bergquist, Mercury stable isotopes reveal the sources and transformations of atmospheric Hg in the high Arctic. *Appl. Geochem.* **131**, 105002 (2021).
41. L. Sun, X. Zhang, J. Zheng, Y. Zheng, D. Yuan, W. Chen, Mercury concentration and isotopic composition on different atmospheric particles (PM10 and PM2.5) in the subtropical coastal suburb of Xiamen Bay, Southern China. *Atmos. Environ.* **261**, 118604 (2021).
42. B. Yu, L. Yang, L. L. Wang, H. W. Liu, C. L. Xiao, Y. Liang, Q. Liu, Y. G. Yin, L. G. Hu, J. B. Shi, G. B. Jiang, New evidence for atmospheric mercury transformations in the marine boundary layer from stable mercury isotopes. *Atmos. Chem. Phys.* **20**, 9713–9723 (2020).
43. C. J. Li, J. B. Chen, H. Angot, W. Zheng, G. T. Shi, M. H. Ding, Z. H. Du, Q. G. Zhang, X. Y. Ma, S. C. Kang, C. D. Xiao, J. W. Ren, D. H. Qin, Seasonal variation of mercury and its isotopes in atmospheric particles at the Coastal Zhongshan Station, Eastern Antarctica. *Environ. Sci. Tech.* **54**, 11344–11355 (2020).
44. X. Fu, X. Yang, Q. Tan, L. Ming, T. Lin, C.-J. Lin, X. Li, X. Feng, Isotopic composition of gaseous elemental mercury in the marine boundary layer of East China Sea. *J. Geophys. Res. Atmos.* **123**, 7656–7669 (2018).
45. A. Y. Kurz, J. D. Blum, M. W. Johnson, K. Nadelhoffer, D. R. Zak, Isotopic composition of mercury deposited via snow into mid-latitude ecosystems. *Sci. Total Environ.* **784**, 147252 (2021).
46. X. Wang, J. Luo, W. Yuan, C.-J. Lin, F. Wang, C. Liu, G. Wang, X. Feng, Global warming accelerates uptake of atmospheric mercury in regions experiencing glacier retreat. *Proc. Natl. Acad. Sci. U.S.A.* **117**, 2049–2055 (2020).
47. S. Huang, L. Sun, T. Zhou, D. Yuan, B. Du, X. Sun, Natural stable isotopic compositions of mercury in aerosols and wet precipitations around a coal-fired power plant in Xiamen, southeast China. *Atmos. Environ.* **173**, 72–80 (2018).
48. M. Enrico, G. Le Roux, N. Marusczak, L. E. Heimburger, A. Claustres, X. W. Fu, R. Y. Sun, J. E. Sonke, Atmospheric mercury transfer to peat bogs dominated by gaseous elemental mercury dry deposition. *Environ. Sci. Tech.* **50**, 2405–2412 (2016).
49. S. Yuan, Y. Zhang, J. Chen, S. Kang, J. Zhang, X. Feng, H. Cai, Z. Wang, Z. Wang, Q. Huang, Large variation of mercury isotope composition during a single precipitation event at Lhasa City, Tibetan Plateau, China. *Procedia Earth Planet. Sci.* **13**, 282–286 (2015).
50. L. S. Sherman, J. D. Blum, J. T. Dvonch, L. E. Gratz, M. S. Landis, The use of Pb, Sr, and Hg isotopes in Great Lakes precipitation as a tool for pollution source attribution. *Sci. Total Environ.* **502**, 362–374 (2015).
51. P. M. Donovan, J. D. Blum, D. Yee, G. E. Gehrke, M. B. Singer, An isotopic record of mercury in San Francisco Bay sediment. *Chem. Geol.* **349–350**, 87–98 (2013).
52. L. S. Sherman, J. D. Blum, T. A. Douglas, A. Steffen, Frost flowers growing in the Arctic ocean-atmosphere–sea ice–snow interface: 2. Mercury exchange between the atmosphere, snow, and frost flowers. *J. Geophys. Res. Atmos.* **117**, D00R10 (2012).
53. L. C. Motta, J. D. Blum, M. W. Johnson, B. P. Umhau, B. N. Popp, S. J. Washburn, J. C. Drazen, C. R. Benitez-Nelson, C. C. S. Hannides, H. G. Close, C. H. Lamborg, Mercury cycling in the North Pacific subtropical gyre as revealed by mercury stable isotope ratios. *Global Biogeochem. Cycles* **33**, 777–794 (2019).
54. S. L. Yuan, J. B. Chen, H. Hintelmann, H. M. Cai, W. Yuan, S. He, K. Zhang, Y. Y. Zhang, Y. L. Liu, Event-based atmospheric precipitation uncovers significant even and odd Hg isotope anomalies associated with the circumpolar vortex. *Environ. Sci. Tech.* **56**, 12713–12722 (2022).
55. X. Xu, X. Feng, H. Lin, P. Zhang, S. Huang, Z. Song, Y. Peng, T.-M. Fu, Y. Zhang, Modeling the high-mercury wet deposition in the southeastern US with WRF-GC-Hg v1.0. *Geosci. Model Dev.* **15**, 3845–3859 (2022).
56. Q. Huang, X. He, W. Huang, J. R. Reinfelder, Mass-independent fractionation of mercury isotopes during photoreduction of soot particle bound Hg(II). *Environ. Sci. Tech.* **55**, 13783–13791 (2021).
57. H. Zhao, B. Meng, G. Sun, C.-J. Lin, X. Feng, J. Sommar, Chemistry and isotope fractionation of divalent mercury during aqueous reduction mediated by selected oxygenated organic ligands. *Environ. Sci. Tech.* **55**, 13376–13386 (2021).
58. W. Zheng, J. D. Demers, X. Lu, B. A. Bergquist, A. D. Anbar, J. D. Blum, B. Gu, Mercury stable isotope fractionation during abiotic dark oxidation in the presence of thiols and natural organic matter. *Environ. Sci. Tech.* **53**, 1853–1862 (2019).
59. W. Zheng, H. Hintelmann, Isotope fractionation of mercury during its photochemical reduction by low-molecular-weight organic compounds. *J. Phys. Chem. A* **114**, 4246–4253 (2010).
60. R. Sun, M. Jiskra, H. M. Amos, Y. Zhang, E. M. Sunderland, J. E. Sonke, Modelling the mercury stable isotope distribution of Earth surface reservoirs: Implications for global Hg cycling. *Geochim. Cosmochim. Acta* **246**, 156–173 (2019).
61. M. L. Wesely, Parameterization of surface resistances to gaseous dry deposition in regional-scale numerical-models. *Atmos. Environ.* **23**, 1293–1304 (1989).
62. S. A. Strode, L. Jaeglé, N. E. Selin, D. J. Jacob, R. J. Park, R. M. Yantosca, R. P. Mason, F. Slemr, Air-sea exchange in the global mercury cycle. *Global Biogeochem. Cycles* **21**, GB1017 (2007).
63. L. Zhang, S. Gong, J. Padro, L. Barrie, A size-segregated particle dry deposition scheme for an atmospheric aerosol module. *Atmos. Environ.* **35**, 549–560 (2001).
64. H. M. Amos, D. J. Jacob, C. D. Holmes, J. A. Fisher, Q. Wang, R. M. Yantosca, E. S. Corbitt, E. Galarneau, A. P. Rutter, M. S. Gustin, A. Steffen, J. J. Schauer, J. A. Graydon, V. L. S. Louis, R. W. Talbot, E. S. Edgerton, Y. Zhang, E. M. Sunderland, Gas-particle partitioning of atmospheric Hg(II) and its effect on global mercury deposition. *Atmos. Chem. Phys.* **12**, 591–603 (2012).
65. H. Y. Liu, D. J. Jacob, I. Bey, R. M. Yantosca, Constraints from ^{210}Pb and ^{7}Be on wet deposition and transport in a global three-dimensional chemical tracer model driven by assimilated meteorological fields. *J. Geophys. Res. Atmos.* **106**, 12109–12128 (2001).
66. M. Santillana, P. Le Sager, D. J. Jacob, M. P. Brenner, An adaptive reduction algorithm for efficient chemical calculations in global atmospheric chemistry models. *Atmos. Environ.* **44**, 4426–4431 (2010).
67. A. Sandu, R. Sander, Technical note: Simulating chemical systems in Fortran90 and Matlab with the Kinetic PreProcessor KPP-2.1. *Atmos. Chem. Phys.* **6**, 187–195 (2006).
68. J. D. Blum, B. A. Bergquist, Reporting of variations in the natural isotopic composition of mercury. *Anal. Bioanal. Chem.* **388**, 353–359 (2007).
69. J. D. Blum, Handbook of environmental isotope. *Geochemistry.*, 229–245 (2012).
70. J. D. Blum, M. W. Johnson, Recent developments in mercury stable isotope analysis. *Rev. Mineral. Geochem.* **82**, 733–757 (2017).
71. W. Zheng, H. Hintelmann, Mercury isotope fractionation during photoreduction in natural water is controlled by its Hg/DOC ratio. *Geochim. Cosmochim. Acta* **73**, 6704–6715 (2009).

72. X. Fu, X. Y. Sun, O. Travnikov, Q. Y. Li, C. Qin, C. A. Cuevas, R. P. Fernandez, A. S. Mahajan, S. X. Wang, T. Wang, A. Saiz-Lopez, Anthropogenic short-lived halogens increase human exposure to mercury contamination due to enhanced mercury oxidation over continents. *Proc. Natl. Acad. Sci. U.S.A.* **121**, e2315058121 (2024).
73. A. Saiz-Lopez, A. U. Acuña, A. S. Mahajan, J. Z. Dávalos, W. Feng, D. Roca-Sanjuán, J. Carmona-García, C. A. Cuevas, D. E. Kinnison, J. C. Gómez Martín, J. S. Francisco, J. M. C. Plane, The chemistry of mercury in the stratosphere. *Geophys. Res. Lett.* **49**, e2022GL097953 (2022).
74. R. Sun, D. G. Streets, H. M. Horowitz, H. M. Amos, G. Liu, V. Perrot, J.-P. Toutain, H. Hintelmann, E. M. Sunderland, J. E. Sonke, Historical (1850–2010) mercury stable isotope inventory from anthropogenic sources to the atmosphere. *Elementa* **4**, 000091 (2016).
75. X. Wang, W. Yuan, C. J. Lin, L. Zhang, H. Zhang, X. Feng, Climate and vegetation as primary drivers for global mercury storage in surface soil. *Environ. Sci. Tech.* **53**, 10665–10675 (2019).
76. D. Obrist, Y. Agnan, M. Jiskra, C. L. Olson, D. P. Colegrove, J. Hueber, C. W. Moore, J. E. Sonke, D. Helmig, Tundra uptake of atmospheric elemental mercury drives Arctic mercury pollution. *Nature* **547**, 201–204 (2017).
77. M. Jiskra, J. G. Wiederhold, U. Skyllberg, R. M. Kronberg, I. Hajdas, R. Kretzschmar, Mercury deposition and re-emission pathways in boreal forest soils investigated with Hg isotope signatures. *Environ. Sci. Tech.* **49**, 7188–7196 (2015).
78. B. Yu, X. W. Fu, R. S. Yin, H. Zhang, X. Wang, C. J. Lin, C. S. Wu, Y. P. Zhang, N. N. He, P. Q. Fu, Z. F. Wang, L. H. Shang, J. Sommar, J. E. Sonke, L. Maurice, B. Guinot, X. B. Feng, Isotopic composition of atmospheric mercury in China: New evidence for sources and transformation processes in air and in vegetation. *Environ. Sci. Tech.* **50**, 9262–9269 (2016).
79. A. Y. Kurz, J. D. Blum, L. E. Gratz, D. A. Jaffe, Contrasting controls on the diel isotopic variation of Hg^0 at two high elevation sites in the Western United States. *Environ. Sci. Tech.* **54**, 10502–10513 (2020).
80. J. E. Sonke, A global model of mass independent mercury stable isotope fractionation. *Geochim. Cosmochim. Acta* **75**, 4577–4590 (2011).
81. X. Fu, C. Liu, H. Zhang, Y. Xu, H. Zhang, J. Li, X. Lyu, G. Zhang, H. Guo, X. Wang, L. Zhang, X. Feng, Isotopic compositions of atmospheric total gaseous mercury in 10 Chinese cities and implications for land surface emissions. *Atmos. Chem. Phys.* **21**, 6721–6734 (2021).
82. B. Yu, L. Yang, H. Liu, C. Xiao, D. Bu, Q. Zhang, J. Fu, Q. Zhang, Z. Cong, Y. Liang, L. Hu, Y. Yin, J. Shi, G. Jiang, Tracing the transboundary transport of mercury to the Tibetan Plateau using atmospheric mercury isotopes. *Environ. Sci. Tech.* **56**, 1568–1577 (2022).
83. B. Yu, L. Yang, H. Liu, R. Yang, J. Fu, P. Wang, Y. Li, C. Xiao, Y. Liang, L. Hu, Q. Zhang, Y. Yin, J. Shi, G. Jiang, Katabatic wind and sea–ice dynamics drive isotopic variations of total gaseous mercury on the Antarctic coast. *Environ. Sci. Tech.* **55**, 6449–6458 (2021).
84. L. S. P. Nguyen, G.-R. Sheu, X. Fu, X. Feng, N.-H. Lin, Isotopic composition of total gaseous mercury at a high-altitude tropical forest site influenced by air masses from the East Asia continent and the Pacific Ocean. *Atmos. Environ.* **246**, 118110 (2021).
85. X. Fu, N. Marusczak, X. Wang, F. Gheusi, J. E. Sonke, Isotopic composition of gaseous elemental mercury in the free troposphere of the Pic du Midi Observatory, France. *Environ. Sci. Tech.* **50**, 5641–5650 (2016).
86. J. D. Demers, L. S. Sherman, J. D. Blum, F. J. Marsik, J. T. Dvonch, Coupling atmospheric mercury isotope ratios and meteorology to identify sources of mercury impacting a coastal urban-industrial region near Pensacola, Florida, USA. *Global Biogeochem. Cycles* **29**, 1689–1705 (2015).
87. L. S. Sherman, J. D. Blum, K. P. Johnson, G. J. Keeler, J. A. Barres, T. A. Douglas, Mass-independent fractionation of mercury isotopes in Arctic snow driven by sunlight. *Nat. Geosci.* **3**, 173–177 (2010).
88. W. Zheng, A. Zhou, S. K. Sahoo, M. R. Nolan, C. M. Ostrander, R. Sun, A. D. Anbar, S. Xiao, J. Chen, Recurrent photic zone euxinia limited ocean oxygenation and animal evolution during the Ediacaran. *Nat. Commun.* **14**, 3920 (2023).
89. X. Wu, X. Fu, H. Zhang, K. Tang, X. Wang, H. Zhang, Q. Deng, L. Zhang, K. Liu, Q. Wu, S. Wang, X. Feng, Changes in atmospheric gaseous elemental mercury concentrations and isotopic compositions at Mt. Changbai during 2015–2021 and Mt. Ailao during 2017–2021 in China. *J. Geophys. Res. Atmos.* **128**, e2022JD037749 (2023).
90. M. T. Tate, S. E. Janssen, R. F. Lepak, L. Flucke, D. P. Krabbenhoft, National-scale assessment of total gaseous mercury isotopes across the United States. *J. Geophys. Res. Atmos.* **128**, 1–15 (2023).
91. B. F. Araujo, S. Osterwalder, N. Szponar, D. Lee, M. V. Petrova, J. B. Pernov, S. Ahmed, L. E. Heimbürger-Boavida, L. Laffont, R. Teisserenc, N. Tananaev, C. Nordstrom, O. Magand, G. Stupple, H. Skov, A. Steffen, B. Bergquist, K. A. Pfaffhuber, J. L. Thomas, S. Scheper, T. Petäjä, A. Dommergue, J. E. Sonke, Mercury isotope evidence for Arctic summertime re-emission of mercury from the cryosphere. *Nat. Commun.* **13**, 4956 (2022).
92. J. Guo, L. Tripathee, S. Kang, Q. Zhang, J. Huang, C. Mani Sharma, P. Chen, R. Paudyal, D. Rupakheti, Atmospheric particle-bound mercury in the northern Indo-Gangetic Plain region: Insights into sources from mercury isotope analysis and influencing factors. *Geosci. Front.* **13**, 101274 (2022).
93. Y. Zhang, P. Zhang, Z. Song, S. Huang, T. Yuan, P. Wu, V. Shah, M. Liu, L. Chen, X. Wang, J. Zhou, Y. Agnan, An updated global mercury budget from a coupled atmosphere-land-ocean model: 40% more re-emissions buffer the effect of primary emission reductions. *One Earth* **6**, 316–325 (2023).
94. J. G. Wiederhold, J. C. Christopher, K. Daniel, I. Infante, B. Bourdon, R. Kretzschmar, Equilibrium mercury isotope fractionation between dissolved Hg(II) species and thiol-bound Hg. *Environ. Sci. Tech.* **44**, 4191–4197 (2010).

Acknowledgments: We thank A. Zhou and C. Li for the helpful discussions and suggestions. **Funding:** This work was supported by National Natural Science Foundation of China (grant nos. 42394094 and 42307331 to Z.S.), the Fundamental Research Funds for the Central Universities - Cemac "GeoX" Interdisciplinary Program (0207-14380209 to Z.S.), and the Collaborative Innovation Center of Climate Change, Jiangsu Province (to Z.S.). **Author contributions:** Conceptualization: Z.S. and Y.Z. Methodology: Z.S., Y.Z., S.H., T.Y., and P.Z. Software: Z.S. and Y.Z. Validation: Z.S. and Y.Z. Formal analysis: Z.S., Y.Z., S.H., P.Z., and T.Y. Investigation: Z.S., Y.Z. and K.T. Resources: Z.S. and Y.Z. Data curation: Z.S. and Y.Z. Writing—original draft: Z.S., K.T., G.S., X.F., W.Z., J.C., and Y.Z. Writing—review and editing: Z.S., S.H., P.Z., T.Y., X.M., K.T., G.S., X.F., R.S., W.Z., J.C., and Y.Z. Visualization: Z.S. Supervision: Z.S. and Y.Z. Project administration: Z.S. and Y.Z. Funding acquisition: Z.S. **Competing interests:** The authors declare that they have no competing interests. **Data and materials availability:** All data needed to evaluate the conclusions in the paper are present in the paper and/or the Supplementary Materials. All model code is available at the research group website (www.ebmg.online/mercury) and Zenodo (https://doi.org/10.5281/zenodo.16605966).

Submitted 30 March 2025
Accepted 18 August 2025
Published 19 September 2025
10.1126/sciadv.adx8401